Solution synthesis and dielectric properties of alumina thin films: understanding the role of the organic additive in film formation

Hoffmann, R. C.; Liedke, M. O.; Butterling, M.; Wagner, A.; Trouilletc, V.; Schneider, J. J.;

Originally published:

June 2021

Dalton Transactions 50(2021)25, 8811-8819

DOI: https://doi.org/10.1039/d1dt01439k

ARTICLE

Solution synthesis and dielectric properties of alumina thin films: Understanding the role of the organic additive in film formation.

Received 00th January 20xx,
Accepted 00th January 20xx

DOI: 10.1039/x0xx00000x

Rudolf C. Hoffmann[a], Maciej O. Liedke[b], Maik Butterling[b], Andreas Wagner[b], Vanessa Trouillet[c], and Jörg J. Schneider*[a]

Alumina thin films are synthesized by combustion synthesis of mixtures of aluminium nitrate (ALN) and methylcarbazate (MCZ). The correlation and interdependence of the ratio of oxidizer and reducing agent on composition, microstructure and dielectric properties of the resulting oxide layers is investigated. Uniform films with low surface roughness result from spincoating and direct heating heating of the thin films. XPS studies reveal almost complete removal of the ligand sphere of the precursors after annealing at higher temperatures. However, a layer of carbonaceous adsorbates exists at the film surface even after calcination. The porosity of the films can be analyzed by means of positron annihilation liftetime studies. In this way the impact of the organic ligand sphere on the resulting porosity is quantified. Samples prepared from ALN alone exhibit mesopores and also larger micropores. In contrast, the formation of mesopores can be inhibited by addition of MCZ. Thus, the dielectric properties are improved by addition of a small amount as well as a large excess of MCZ (MCZ:ALN = 0.67 or 2.5). Medium concentrations of MCZ (MCZ:ALN =1.0 or 1.5) lead to films with lower performance, though. This indicates two opposing effects of the organic additive. Removal of organic residues in the form of combustion gases is potentially detrimental. Larger amounts of MCZ, however, cause condensation reactions in the precusor mixture, which improves the microstructure. In this way films (thickness ~140 nm) with a dielectric constant κ of 9.7 and a dielectric loss tan δ below 0.015 can be achieved.

Introduction

Solution combustion synthesis (SCS) of molecular precursors has been proposed as an alternative route to the sol-gel process for the deposition of metal oxide films from solution.[1,2] The employed reaction mixtures contain a combination of oxidizer and reducing agent, such as a metal nitrate and an organic component. In this way, a highly exothermal ceramisation reaction is achieved and the overall processing temperature for thin-film formation is reduced.[3,4] The relative amount of the two components ("fuel to oxidizer ratio") is a trade-off between the increase in generated heat of combustion and possible detrimental effects like excess contamination of the generated films by excess decomposition products from the precursor molecules. The functional oxide layer is only obtained after the deposition of a wet-film in a further step, which typically involves thermal or UV treatment.[5] The removal of organic residues by decomposition or combustion causes the evolution of gaseous reaction products and leads to formation of porosity and shrinkage.[6] That said, the exact function of the organic counterpart, certainly exceeds the role of a mere reducing agent during combustion. The influence occurs on all stages of the deposition process and has an impact on the resulting morphology and microstructure of the resulting oxide layer. Firstly, the type and the amount of the organic component affects the wetting behavior of the coating solution on the proposed substrates.[7,8] More importantly, basic additives will induce condensation processes generating M-O-M or M-OH-M linkages in solution or the wet-film, i.e. formation of sol or gels.[9,10] This is particularly advantageous as the ceramic yield is increased, which limits shrinkage during calcination.[11] These few examples already show, that a control and understanding of the chemical nature of the interaction between metal nitrate and organic molecules in the precursor solution as well as film-formation reaction of the precursor gels is required.[12,13] In addition investigations of the decomposition pathway as well as the oxide formation process are highly important for developing the synthetic process for thin film manufacturing.[8,13]

Metal oxide dielectric materials are a key element in thin film electronic systems. The two most critical characteristics are high areal capacitance and ideal electrical insulation.[14] This definitively narrows the available choice, as a high dielectric constant and a large band gap are required at the same time, which is only the case in a small number of metal oxides. Furthermore, a suitable dielectric should be amorphous with a smooth surface and low interface defect density with the semiconductor.[2,14] A good candidate, which fulfills all of these

[a] *Eduard-Zintl-Institut für Anorganische und Physikalische Chemie, Technische Universität Darmstadt, Alarich-Weiss-Straße 12, 64287 Darmstadt, Germany*
[b] *Institute of Radiation Physics, Helmholtz-Zentrum Dresden-Rossendorf, Bautzner Landstraße 400, 01328 Dresden, Germany*
[c] *Institute for Applied Materials (IAM-ESS) and Karlsruhe Nano Micro Facility (KNMF), Karlsruhe Institute of Technology (KIT), Hermann-von-Helmholtz-Platz 1, 76344 Eggenstein- Leopoldshafen, Germany.*

Electronic Supplementary Information (ESI) available: Additional figures. See DOI: 10.1039/x0xx00000x

Dedicated to Prof. H.G. Schnöckel on the occasion of his 80 birthday.

criteria is aluminum oxide.[15] Thus, consequently there is great interest in synthetic approaches for such thin films.

SCS was applied by different groups using mixtures of aluminium nitrate and urea in methoxyethanol. Interestingly, very different ratios, i.e. 1:2.5 [16,17] and 1:6 [18] were chosen. The extremely fuel rich composition leads to drastically better results. Unfortunately, no explanation was evident and a systematic comparison on the influence of the relative amount of the educts is missing. On the other hand aluminium oxide powders have successfully been synthesized by means of SCS for decades.[19] So far a plethora of reducing agents was successfully tested for potential use. In SCS. In a direct comparison (Scheme 1) between urea and carbohydrazide or methylcarbazate, the latter lead to lower ignition temperatures, but also the generation of less heat of combustion.[20] This resulted in larger particles with lower specific surface area. Whereas this finding might be undesirable for the synthesis of ultra-small nanoparticles, it might hint at a possible improvement for the synthesis of dense and less porous thin films.[20,21]

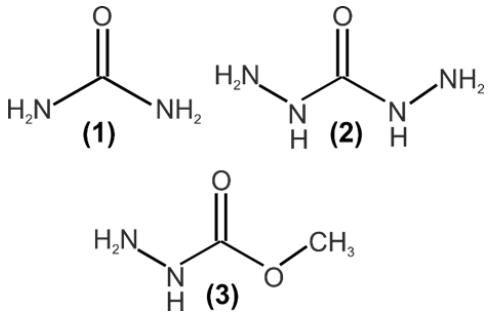

Scheme 1: Structural formula of various fuels in SCS. (1) urea, (2) carbohydrazide and (3) methylcarbazate.

In this work SCS of alumina thin films using aluminium nitrate nonahydrate (ALN) and methyl carbazate (MCZ) is investigated. Emphasis is put on elucidating the impact of the fuel/oxidizer ratio on the resulting microstructure and morphology of the dielectric films and the corresponding dielectric performance of the dielectric. Hereby, high-resolution transmission electron microscopy (HR-TEM) as well as positron life-time measurements (PALS) are used to gain insight into the microstructure of the alumina thin films. In addition, the species obtained in solution and in the wet film, will also be elucidated. Finally, the dielectric properties of the solution processed alumina films are studied using a metal/insulator/metal device. Overall, an attempt will be made to get a broad picture involving all steps in the combustion process for metal oxide film formation.

Results and discussion

Wet film formation and thermal decomposition of precursor

Thin films are prepared from solutions of ALN and MCZ in methoxyethanol by spincoating and subsequent calcination. The molar ratio Φ_S for the stoichiometric composition of the mixture with respect to the combustion reaction can be calculated using the chemical valence approach of *Jain et al.*,[22] yielding a composition of MCZ:ALN = 0.67 (Supplement Scheme 1). Thus, in this work molar ratios Φ_M MCZ:ALN ranging from 0.0 to 3.0 are taken into account. Furthermore, two aluminium ion concentrations of 0.4 and 0.2 M (i.e. ~15 or 7.5 weight % of ALN) are compared. Solutions with molar ratios Φ_M from 0.0 to 2.5 are stable over longer periods of time (minimum eight hours), whereas with higher amounts of MCZ gelation is observed within a few hours. Therefore, the solutions are investigated by means of Dynamic Light Scattering (DLS). Interestingly, the addition of MCZ leads to the formation of nanoscalic particles in all investigated concentration regimes (Figure 1a). For the lowest contents of MCZ the size remained constant, whereas rather slow particle growth is observed for Φ_M = 2.5 and rapid growth for Φ_M = 3.0.

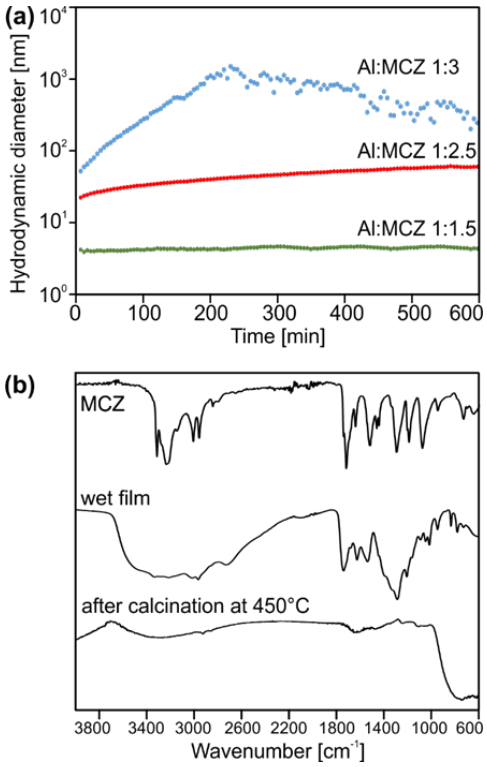

Figure 1: (a) Time dependence of the size of particles in solutions containing various ratios of ALN (0.4 M) and MCZ. (b) AT-IR spectra of MCZ as well as films from precursor mixture (ALN 0.4 M, MCZ:ALN = 2.5) before (wet film) and after calcination at 450 °C.

Wet films obtained after spincoating are investigated by Attenuated Total Reflection Infrared Spectroscopy (ATR-IR) (Figure 1b). The signals differ significantly from those of pure MCZ. Vibrations related to ν(C=O) and ν(-NH_2-C=O) are shifted to lower wavelengths and additional signals characteristic for Al-OH groups at 1130 cm^{-1} occur. This corresponds to earlier investigations in the system ALN-urea and hint at beginning condensation reactions, i.e. olations.[23] Peaks arising from Al-O units, in the range at 600-700 cm^{-1} and i.e. due to oxolation processes can however, only be found after additional calcination at higher temperatures.

In order to investigate the decomposition mechanism, the solvent is evaporated from the before-mentioned solution and thermogravimetric analysis coupled with infrared spectroscopy (TG/IR) is carried out (Supplement Figure 1, Figure 2). In comparison to the thermal decay of pure ALN without further additive,[23,24] the onset of the decomposition is shifted to elevated temperatures with increased addition of MCZ. Furthermore, two clearly distinct decomposition steps are formed. The thermal decay is complete above ~240 °C, whereby a constant residual mass is reached slightly above ~290 °C in all investigated cases.

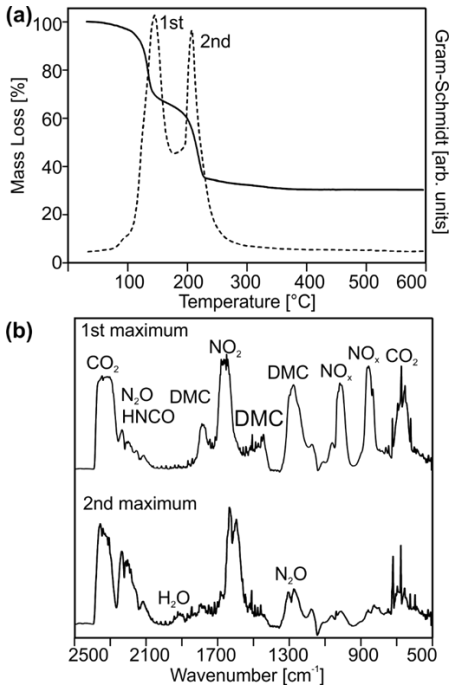

Figure 2: (a) Mass loss (straight line) of precursor mixture (ALN 0.4 M, MCZ:ALN = 2.5) and corresponding Gram-Schmidt curve (dotted). (b) IR spectra recorded at the maxima of the Gram-Schmidt curve in (a).

An analysis of the gaseous decomposition products is carried out by means of IR spectroscopy. The attribution of the plethora of peaks is not perfectly straight forward as a mixture of different gases is present. It is possible, however, to identify a number of small molecules like carbon dioxide (CO_2) as well as dinitrogen oxide (N_2O) and isocyanic acid (HNCO), but also the nitrogen oxides (NO_x), which are expected from combustion and comproportionation reactions.[25,26] However, ammonia or hydrazine are definitely not formed. A carbonyl containing compound can be found, especially under high ratios of MCZ:ALN applied. Thereby ν(C=O) is present at comparably high wavenumbers, e.g. 1757 cm^{-1}, indicating that further electron withdrawing groups are linked to the carbonyl carbon. Products resulting from a C-N or N-N cleavage (as might be expected from calculations on cyclical transition states in the gas phase decomposition of methylcarbazate[27]) cannot be identified, though. Instead on basis of the signals present in the fingerprint region (at 1280 cm^{-1}) an unambiguous attribution to dimethyl carbonate (DMC) is possible. Interestingly, a comparable rearrangement under formation of DMC has been found by our group for the decomposition of zinc complexes with functionalized malonic acid esters.[26,28] Possibly, this is a general effect of the methoxy-formyl functionality -CO(OCH_3), which occurs due to an enhanced kinetic stability of DMC. This view is supported by the finding that even for very high ratios of MCZ:ALN in the precursor mixtures, still NO_x is found in the reaction products, which could act as an oxidizing agent.

Topology and microstructure of alumina thin films

Films obtained from mixtures of different MCZ:ALN ratios after calcination appear very uniform with homogeneous surface coverage. Atomic force microscopy (AFM) reveals a very smooth surface topology. (Figure 3) A particulate morphology becomes visible at higher magnification in SEM micrographs in cross sections of such films (Supplement Figure 2). Lighter contrast areas may be indicative for cracks as well as pinholes. Such microstructure is not only observed for coatings from dispersions of nanoparticles, but also for precursor-derived ceramics, e.g. dielectrics obtained from complexes with oximato ligands. [1, 2] In a more specific approach cross sections are prepared using the Focussed Ion Beam (FIB) preparation technique and characterized using High-Resolution Transmission electron Microscopy (HRTEM) (Figure 4, Supplement Figure 3). X-Ray diffraction of films obtained on quartz appear amorphous even after calcination at 500 °C (Supplement Figure 4). This is not surprising as films synthesized from the decomposition of ALN alone are known to be amorphous up to temperatures well above 550 °C. [3, 4] Either the crystalline particles are too small for a distinct detection by X-ray diffraction, or the crystallinity is induced by the electron beam or sample preparation.

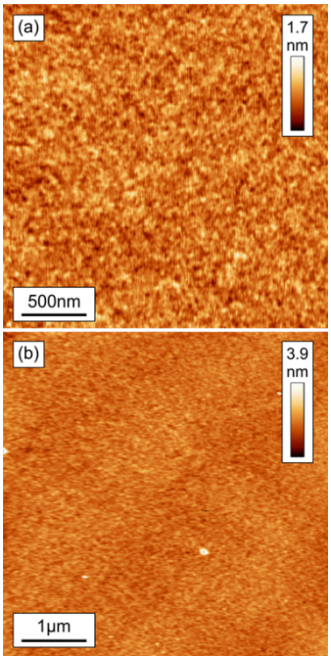

Figure 3: AFM image of the topography of an alumina film on a silicon substrate obtained from spincoating of the precursor mixture (ALN 0.4 M, MCZ:ALN = 2.5) and annealing at 450 °C. (a) and (b) show different magnifications. (Thickness ~ 145 nm, RMS 0.2 nm)

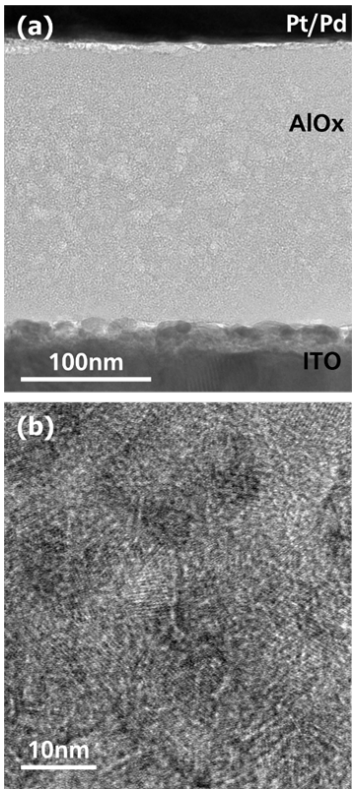

Figure 4: (a) HRTEM micrograph of cross-section prepared by FIB of alumina film obtained from precursor mixture (ALN 0.4 M, MCZ:ALN = 2.5) after annealing at 450 °C. (b) Image at higher magnification of the same sample.

UV/VIS spectra show highly transparent films (Supplement Figure 5). It is not possible to determine the band-gap of aluminium oxide using optical spectroscopy, which lies well below this wavelength regime. Crystalline α-Al_2O_3 has a band-gap of 8.6 eV,[32] whereby this is significantly reduced in amorphous films to 6.9 eV.[33] In any case absorption edges at about ~ 4.9 eV in some publications[16] presumably result from residual organic or defects.[34]

XPS investigations elucidate the chemical composition of the films and especially the eventual presence of organic residues (Figure 5, Supplement Figure 6). Films synthesized from mixtures of ALN and MCZ after annealing at 250 °C (**1**) as well as 500 °C (**2**) are measured. For comparison also a film from ALN without additives (**3**) is investigated, which could nevertheless exhibit residues from the solvent. In order to have results from a sample with no organic contributions at all, a specimen from oxidation of metallic aluminium (**4**) is also included.

Top surfaces are measured and depth profiles are conducted in order to get information within the layer. All samples show some usual environmental contamination evidenced by the C 1s region before sputtering. This surface contamination can be then removed whereas in the case of **(1)**, further carbon species are still detected in the depth. In addition (**1**) exhibits three N 1s components before sputtering, namely NO_3^- (407.3 eV), NO_2 groups (403.6 eV) and amine/amide groups (400.0 eV).[35] These signals, however, vanish after a few cycles of sputtering. This could hint at a possible fixation of decomposition products of MCZ as well as rest of nitrate on the surface of the deposited film.[36,37]

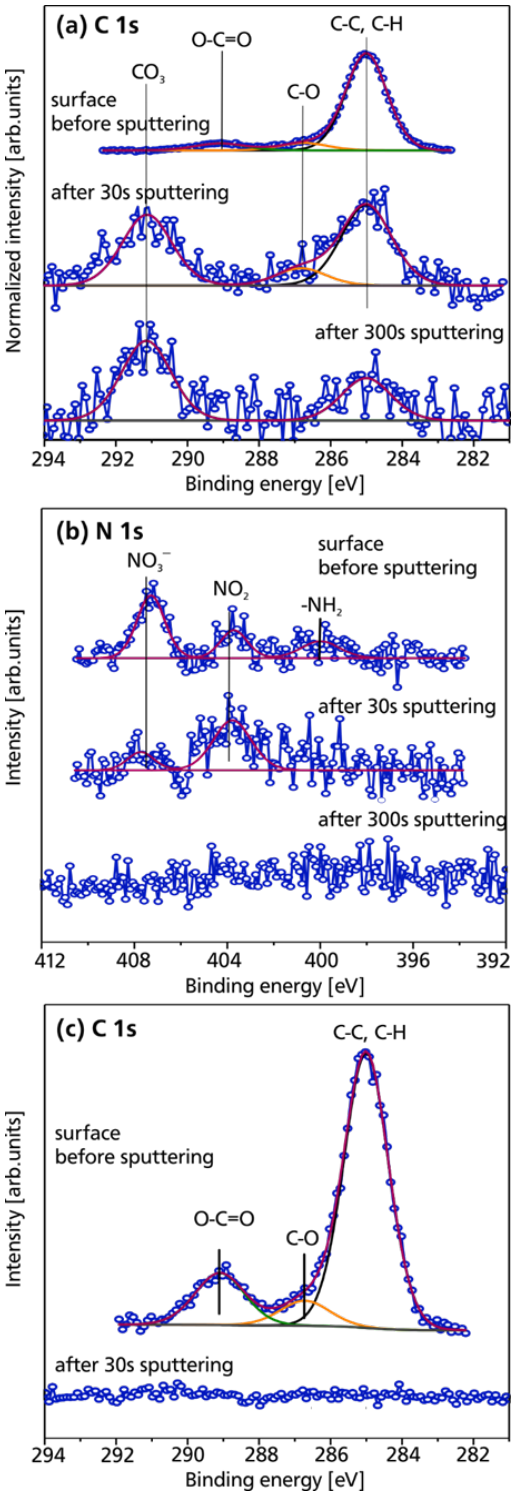

Figure 5: XPS spectra depicting (a) C 1s and (b) N 1s region of (**1**) as well as (c) C 1s region of (**2**).

In agreement with the TG analysis, the removal of carbonaceous species in (**1**) is incomplete but represents less than 2.5 at.% of the layer composition. O 1s in all samples can be deconvoluted in two peaks, one at 531.5 eV and a second one at 533.5 eV. This reflects respectively the presence of aluminium in an oxidic

(O^{2-}) as well as hydroxylic (OH^-) coordination environment or possibly even from carbon species in the case of (**1**). [35,38] It can be noted that only (**1**) and (**2**) show a ratio hydroxide / oxide of ~ 1/10 in contrary to (**3**) and (**4**) which contain almost only Al_2O_3. Nevertheless, for all samples, Al_2O_3 is the predominant species with a ratio O (531.5 eV) / Al of 1.5.

Dielectric properties

Capacitors are fabricated in order to determine the dielectric properties. Thereby an established design (metal/insulator/metal MIM) for the set-up is employed (Figure 6). Initially a higher aluminium concentration, i.e. 0.4 M, is chosen, since this allows the deposition of thicker films using less iterations of spincoating and subsequent calcinations. Annealing at 450 °C in air is used to achieve complete ceramisation. Capacitors are fully prepared under environmental conditions and characterized without further annealing under argon. Breakdown measurements indicate that a minimum thickness of ~ 100 nm is required for sufficient insulating properties (Supplement Figure 7).

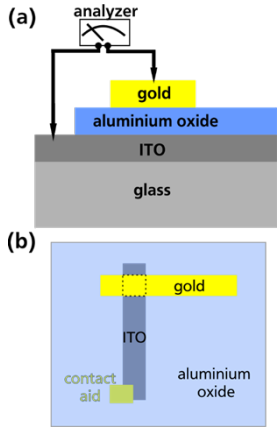

Figure 6: Schematic set-up of a MIM capacitor. (a) Cross section indicating layer arrangement and substrate configuration. (b) Top view illustrating the perpendicular arrangement of the electrodes and the position of the contact aid. The overlapping area is highlighted by a dashed square.

Typically, maximum dielectric strengths of 2.0 MV/cm and leakage current densities well below 10^{-8} A (at 1.0 MV/cm) are obtained. Such performance parameters are considered appropriate for the use in thin film transistors.[39] These values did not vary significantly upon changing the MCZ:ALN ratio. Samples without addition of MCZ (κ 6.8 and tan δ 0.087) however exhibited lower dielectric strength and higher leakage current densities. Dielectric constant κ and loss tangent tan δ are determined as a function of the MCZ:ALN ratio (all values extracted at 105 Hz). The best results are achieved for MCZ:ALN = 0.75 or 2.5 with κ 7.6 and tan δ 0.034 as well as κ 8.4 and tan δ 0.014, respectively (Figure 7a). An intermediate MCZ:ALN ratio of 1.5 leads to a detrimental performance (κ 6.3 and tan δ 0.105).

In a second series of investigations, a lower aluminium concentration, i.e. 0.2 is used in order to improve the dielectric behaviour, whereby the MCZ:ALN ratio is maintained. For the deposition of dielectrics but also for semiconductors from solution porosity can be lowered and more homogeneous layers are obtained by applying more layers with lower precursor concentrations.[40,41] At the same time cracks as well as pinholes are filled by subsequent deposition in such multilayer arrangements. In this way defects are healed and the overall performance improves.[42] Actually an increase of the dielectric constant to κ of 9.7 and a dielectric loss tan δ 0.015 (Figure 7b) is obtained. In both cases dielectric performance parameters are not significantly affected by the film thickness. Furthermore, the observed frequency dispersion is low. This underlines the quality of the aluminium oxide films in this work, as a contrasting behaviour can be observed for solution deposited dielectrics.[29,40]

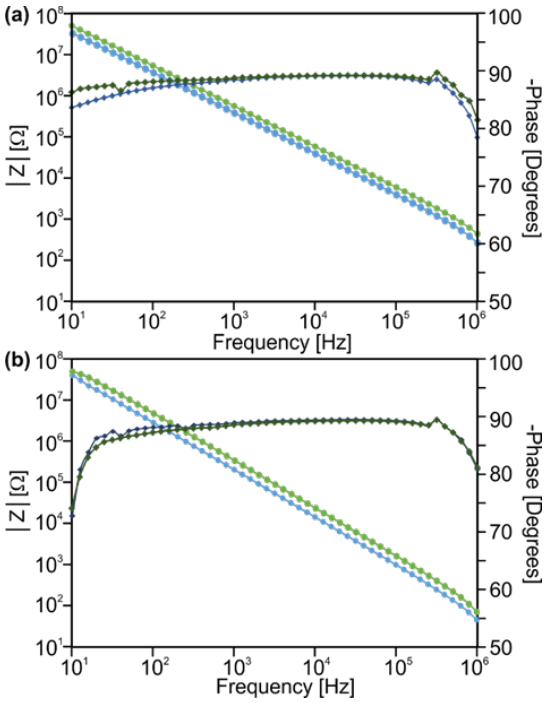

Figure 7: Bode Plots for aluminium oxide films obtained from MCZ:ALN mixtures with a molar ratio of 2.5. (a) ALN 0.4 M and (b) ALN 0.2 M. Green and blue curves represent films with ~210 nm as well as ~145 nm thickness, respectively. Top electrodes with 1000 µm width and bottom ITO electrodes with 250 µm width in all cases.

Microstructure and point defect analysis by PALS

In an attempt to correlate the dielectric properties to the intrinsic microstructure of the alumina thin films positron annihilation lifetime spectroscopy (PALS) is helpful (Supplement Figure 8). Samples are prepared by consecutive spincoating and annealing at 450 °C of six layers of the precursor mixture on silicon substrates. The curve fitting of these PALS spectra is carried out with 5 lifetime components (τ_1-τ_5) (Supplement Figure 9).

The 1st contribution (τ_1) ranges from values of 0.1 to 0.3 ns in dependence of the MCZ:ALN ratio. In earlier investigations components with comparable lifetimes are observed. The value is influenced by impurities,[43,44] the amount of residual hydroxylation[45] as well as the crystallinity or amorphicity[44] of the sample and most interestingly it has been reported that any addition of carbon to α-alumina and its subsequent calcination

affects this parameter.[46] Thus, the differences between films obtained solely from ALN and those with addition of MCZ can be explained by the reducing behavior of the latter. Hereby, not only the value of τ_1 is shifted, but also the relative intensity I_1 is significantly increased. The lifetime component τ_1 is typically assigned to aluminium vacancies (V_{Al}) or larger defect clusters associated therewith.43,46 In addition, further contribution (τ_2-τ_5) with longer lifetimes are found. These contain valuable information about larger voids and the porosity of the film (Figure 8).[43,44] Thus, the 2nd component (τ_2) corresponds to small micropores (about 0.3 nm in diameter). The relative intensity is highest, if no MCZ is added, whereby this free volume size also dominates in the sample (I_2≈70%). Furthermore, a clear gradient with respect to the depth profile is observed here. In the other specimen the lifetime component representing about 40% positrons annihilate due to this particular defect. The 3rd and the 4th component (τ_3 and τ_4) correspond to micropores with ~ 0.5nm and ~1 nm size and a relative abundance of 20% or 10%, respectively. Finally, the 5th contribution is attributed to mesopores (> 1 nm).

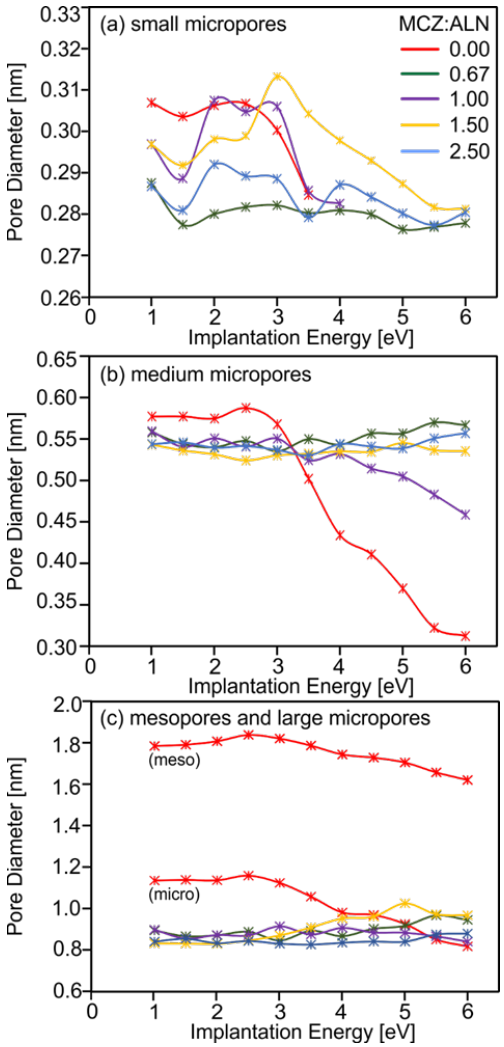

Figure 8: Pore sizes obtained from positron lifetime components τ_2-τ_5 as a function of implantation energy of alumina films on silicon substrates obtained from precursor mixtures with various MCZ:ALN ratios. (a) small micropores, (b) medium micropores as well as (c) large micropores and mesopores.

Relative intensities below 1% can be considered as residuals, hence can be neglected for samples with a MCZ addition. In contrast to that, a distinct contribution can be found in the sample obtained solely from ALN without any MCZ addition.

Conclusions

Aluminium oxide thin films can be obtained by solution combustion synthesis using mixtures of aluminium nitrate nonahydrate and methyl carbazate. Spincoating of solutions in methoxyethanol leads to functional capacitors. The dielectric performance is clearly influenced by the employed MCZ:ALN ratio Φ_M. However, several opposing trends must be taken into account. Thus, improvement of the dielectric behavior is only observed with lower (Φ_M ~ 0.75) as well as with the highest (Φ_M ~ 2.0) relative amounts of MCZ. PALS clearly reveals that addition of MCZ prevents the formation of mesopores in the resulting aluminium oxide films. Furthermore, higher amounts of MCZ favor olation reactions (gelation) in the wet film, which is supposed to enhance the ceramic yield. That said, with intermediate MCZ:ALN ratios (Φ_M ~ 1.5) no obvious improvement with respect to samples obtained solely from ALN becomes visible. In this case the beneficial effects of using an additive are not able to overcome the drawbacks from having to remove the organic content by pyrolysis. In any case gaseous reaction products evolve during combustion which leads to shrinkage and formation of porosity. Surprisingly, TG coupled with IR measurements reveal that the expected com-proportionation reactions do not take place. Instead, kinetically stable intermediates are formed, i.e. the combustion remains incomplete. Our findings question an assessment of solution combustion synthesis merely on the basis of thermodynamic data for an idealized ceramisation process, which is frequently found in the literature. A comparison of various reducing agents ("fuels") should only be possible in a meaningful way by comprehensive experimental investigations.

Experimental

Preparation of precursor mixture and coating of substrates

Coating solutions are prepared by disolving aluminium nitrate nonahydrate (ALN) and methylcarbazate (MCZ) separarely in methoxyethanol. The solutions are mixed and run through a syringe filter (0.2 µm pore size). Carrying out the solution process separately is required in order to avoid local concentration excesses and undesired pre-gelation. The resulting precursor mixtures have ALN concentrations of 0.4 or 0.2 M. The MCZ:ALN ratio is varied from 0 to 2.5. Films were produced by spincoating (30 s at 2000 rpm) of the precursor mixture on quartz, silicon or indium-tin-oxide (ITO), coated glass slides (all substrates 1.5 x 1.5 cm^2) and subsequent annealing on a hot plate. Thicker films could be obtained by iteration of the described coating procedure.

Device fabrication

The MIM capacitor was fabricated by using patterned indium tin oxide (ITO) on glass (140 nm, OLED grade) as bottom electrode. A sacrificial titanium or chromium/gold bilayer (3 nm/40 nm) of square geometry was deposited at an edge of the ITO film by sputtering using a shadow mask. Thereafter the precursor mixture was spin coated and annealed. After the deposition of the dielectric material, gold electrodes (50 nm) were deposited on these dielectric films using a shadow mask by sputter evaporation using a platinum metal source. ITO and platinum electrodes formed perpendicularly overlapping strips with different intersections of varying area size. The contact probe was attached to the ITO electrode through the sacrificial gold layer. Due to this procedure the dielectric film is not punctured or damaged by mechanical cracking.

Material Characterization

(HRTEM/FIB) FEI Tecnai G2 F20, with an operating voltage of 200 keV. FIB preparation carried out using an FEI Helios NanoLab 460F1 FIB-SEM, followed by coating with a platinum layer. Atomic Force Microscopy (AFM): CP-II (Bruker-Veeco), 0.5 Hz, silicon cantilevers. UV/VIS Spectroscopy: Thermo Scientific Evolution 600. X-Ray diffraction (XRD): Miniflex 600 (Rigaku), Cu-Kα radiation, 600 W in Bragg-Brentano geometry. Scanning electron microscopy (SEM): Micrographs were obtained with an XL Series, Philips, XL30 FEG. Ellipsometry: Woollam M-2000 V spectrometer (spectral range 370–1690 cm^{-1}) using the CompleteEASE software (version 6.29). X-Ray photoelectron spectroscopy (XPS): Thermo Fisher Scientific, East Grinstead, UK. A monochromated Al Kα X-ray source with a spot size of 400 µm is used. The K alpha+ charge compensation system is used during the analysis, using electrons of 8 eV energy and low-energy argon ions to prevent any localized charge build-up. The spectra are fitted with one or more Voigt profiles (uncertainty: ±0.2 eV) and Scofield sensitivity factors were applied for quantification. All spectra are referenced to the C 1s peak of hydrocarbons at 285.0 eV by means of the well-known photoelectron peaks of metallic Cu, Ag and Au, respectively. For depth profiling, a gun delivering Argon ions with 3keV energy is used.

Positron annihilation spectroscopy (PAS)

The positron lifetime investigations are performed at the Mono-energetic Positron Spectroscopy (MePS) beamline, which is the end station of the radiation source ELBE (Electron Linac for beams with high Brilliance and low Emittance) at HZDR, Germany. A digital lifetime $CrBr_3$ scintillator detector with homemade software operating on SPDevices ADQ14DC-2X hardware with 14-bit vertical resolution, 2 GS/s horizontal resolution, and with a time resolution function down to about 230 ps are utilized. All spectra contain at least $5 \cdot 10^6$ counts. The positron lifetime spectra represent a sum of time-dependent exponential decays $N(t)= \sum_i I_i/\tau_i \cdot \exp(-t/\tau_i)$ convoluted with Gaussian's functions describing the spectrometer timing resolution. Spectra analysis is conducted using the non-linearly least-squared based package PALSfit fitting software. An yttria-stabilized zirconia reference sample with well-defined single component positron lifetime, $\tau \approx 181$ ps, is taken as a correction spectrum to account for undesirable background by means of subtracting not related to the sample positron lifetime components during the fitting procedure: ~ 400-900 ps (< 5 %) and < 55 ns (< 1 %) depending on positron implantation energy.

Electrical characterization

Impedance measurements were carried out using ModuLab MTS System (Solartron Analytical Ltd.) equipped with a probe station (Cascade Microtech, Inc). Measurements were carried out from 1 MHz to 1 mHz at amplitudes of 500 mA.

Conflicts of interest

There are no conflicts to declare.

Acknowledgements

Positron annihilation studies were carried out at ELBE set up at the Helmholtz-Zentrum Dresden-Rossendorff e.V (project 20202048-ST). Technical support of E. Hirschmann and A. G. Attallah is acknowledged. TEM investigations were performed at ERC Jülich under contract ERC-TUD1. We acknowledge assistance of J. Engstler (TEM) and S. Heinschke (elipsometry) both at TUDa. Funding through DFG under the project SCHN375/36-1 is acknowledged with gratitude.

References

1 W. Marchal, D. De Sloovere, M. Daenen, M. K. Van Bael and A. Hardy, *Chem. Eur. J.*, 2020, **26**, 9070-9083.
2 S. Park, C. H. Kim, W. J. Lee, S. Sung and M. H. Yoon, *Mater. Sci. Eng. R Rep.*, 2017, **114**, 1-22.
3 E. Carlos, R. Martins, E. Fortunato and R. Branquinho, *Chem. Eur. J.*, 2020, **26**, 9099-9125.
4 E. A. Cochran, K. N. Woods, D. W. Johnson, C. J. Page and S. W. Boettcher, *J. Mater Chem. A*, 2019, **7**, 24124-24149.
5 A. Mancinelli, S. Bolat, J. Kim, Y. E. Romanyuk and D. Briand, *ACS Appl. Electron. Mater.*, 2020, **2**, 3141-3151.
6 I. Bretos, S. Diodati, R. Jiménez, F. Tajoli, J. Ricote, G. Bragaggia, M. Franca, M. L. Calzada and S. Gross, *Chem. Eur. J.*, 2020, **26**, 9157-9179.
7 A. Nadarajah, M. Z. B. Wu, K. Archila, M. G. Kast, A. M. Smith, T. H. Chiang, D. A. Keszler, J. F. Wager and S. W. Boettcher, *Chem. Mater.*, 2015, **27**, 5587-5596.
8 X. Zhuang, S. Patel, C. Zhang, B. Wang, Y. Chen, H. Liu, V. P. Dravid, J. Yu, Y.-Y. Hu, W. Huang, A. Facchetti and T. J. Marks, *J. Am. Chem. Soc.*, 2020, **142**, 12440-12452.
9 J.-W. Jo, Y.-H. Kim, J. Park, J. S. Heo, S. Hwang, W.-J. Lee, M.-H. Yoon, M.-G. Kim and S. K. Park, *ACS Appl. Mater. Interfaces*, 2017, **9**, 35114-35124.
10 R. P. Oleksak, R. E. Ruther, F. Luo, J. M. Amador, S. R. Decker, M. N. Jackson, J. R. Motley, J. K. Stowers, D. W. Johnson, E. L. Garfunkel, D. A. Keszler and G. S. Herman, *ACS Appl. Nano Mater.*, 2018, **1**, 4548-4556.
11 R. C. Hoffmann, M. Kaloumenos, E. Erdem, S. Weber and J. J. Schneider, *Eur. J. Inorg. Chem.*, 2014, 5554-5560.
12 J. Cui, M. G. Kast, B. A. Hammann, Y. Afriyie, K. N. Woods, P. N. Plassmeyer, C. K. Perkins, Z. L. Ma, D. A. Keszler, C. J. Page,

S. W. Boettcher and S. E. Hayes, *Chem. Mater.*, 2018, **30**, 7456-7463.
13 B. H. Wang, M. J. Leonardi, W. Huang, Y. Chen, L. Zeng, B. J. Eckstein, T. J. Marks and A. Facchetti, *Adv. Electron. Mater.*, 2019, **5**, 1900540.
14 A. Liu, H. H. Zhu, H. B. Sun, Y. Xu and Y. Y. Noh, *Adv. Mater.*, 2018, **30**, 1706364.
15 J. W. Park, B. H. Kang and H. J. Kim, *Adv. Funct. Mater.*, 2020, **30**, 1904632.
16 R. Branquinho, D. Salgueiro, L. Santos, P. Barquinha, L. Pereira, R. Martins and E. Fortunato, *ACS Appl. Mater. Interfaces*, 2014, **6**, 19592-19599.
17 E. Carlos, R. Branquinho, A. Kiazadeh, J. Martins, P. Barquinha, R. Martins and E. Fortunato, *ACS Appl. Mater. Interfaces*, 2017, **9**, 40428-40437.
18 N. Koslowski, S. Sanctis, R. C. Hoffmann, M. Bruns and J. J. Schneider, *J. Mater. Chem. C*, 2019, **7**, 1048-1056.
19 K. Frikha, L. Limousy, J. Bouaziz, S. Bennici, K. Chaari and M. Jeguirim, C. R. Chim., 2019, **22**, 206-219.
20 C. C. Chen and K. T. Huang, J. Mater. Res., 2005, **20**, 424-431.
21 C. R. Lee, H. W. Lee, J. S. Song, W. W. Kim and S. Park, J. Mater. Synthesis Process. 2001, **9**, 281-286.
22 S. R. Jain, *Propellants Explos. Pyrotech*., 1987, **12**, 188-195.
23 V. D. Zhuravlev, V. G. Bamburov, A. R. Beketov, L. A. Perelyaeva, I. V. Baklanova, O. V. Sivtsova, V. G. Vasil'ev, E. V. Vladimirova, V. G. Shevchenko and I. G. Grigorov, *Ceram. Int.*, 2013, **39**, 1379-1384.
24 B. Pacewska and M. Keshr, *Thermochim. Acta*, 2002, **385**, 73-80.
25 S. Desilets, P. Brousseau, D. Chamberland, S. Singh, H. T. Feng, R. Turcotte, K. Armstrong and J. Anderson, Thermochim. Acta, 2011, **521**, 59-65.
26 R. C. Hoffmann and J. J. Schneider, *Eur. J. Inorg. Chem.*, 2015, 4254-4259.
27 A. Herize, J. R. Mora, J. Lezama, E. Marquez, T. Córdova and G. Chuchani, *J. Phys. Org. Chem.*, 2009, **22**, 170-176.
28 R. C. Hoffmann and J. J. Schneider, *Eur. J. Inorg. Chem.*, 2014, 2014, 2241-2247.
29 M. Kaloumenos, P. Pacak, R. Hoffmann, D. Spiehl, K. Hofmann and K. Bonrad, *RSC Advances*, 2015, **5**, 107608-107615.
30 J. J. Schneider, R. C. Hoffmann, A. Issanin and S. Dilfer, *Mater. Sci. Eng. B-Adv.*, 2011, **176**, 965-971.
31 I. F. Myronyuk, V. I. Mandzyuk, V. M. Sachko and V. M. Gun'ko, *Nanoscale Res. Lett.*, 2016, **11**, 153.
32 T. T. Song, M. Yang, J. W. Chai, M. Callsen, J. Zhou, T. Yang, Z. Zhang, J. S. Pan, D. Z. Chi, Y. P. Feng and S. J. Wang, *Sci. Rep.*, 2016, **6**, 29221.
33 C. Fares, F. Ren, M. J. Tadjer, J. Woodward, M. A. Mastro, B. N. Feigelson, C. R. Eddy and S. J. Pearton, *Appl. Phys. Lett.*, 2020, **117**, 182103.
34 V. A. Pustovarov, V. S. Aliev, T. V. Perevalov, V. A. Gritsenko and A. P. Eliseev, *J. Exper. Theo. Phys.*, 2010, **111**, 989-995.
35 N. Koslowski, V. Trouillet and J. J. Schneider, *J. Mater. Chem. C*, 2020, **8**, 8521-8530.
36 J. Baltrusaitis, P. M. Jayaweera and V. H. Grassian, *Phys. Chem. Chem. Phys.*, 2009, **11**, 8295-8305.
37 M. N. Romanias, A. El Zein and Y. Bedjanian, *J. Photochem. Photobiol. A*, 2012, **250**, 50-57.
38 R. C. Hoffmann, S. Sanctis, E. Erdem, S. Weber and J. J. Schneider, *J. Mater. Chem. C*, 2016, **4**, 7345-7352.
39 C. K. Perkins, M. A. Jenkins, T. H. Chiang, R. H. Mansergh, V. Gouliouk, N. Kenane, J. F. Wager, J. F. Conley and D. A. Keszler, *ACS Appl. Mater. Interfaces*, 2018, **10**, 36082-36087.
40 M. Kaloumenos, K. Hofmann, D. Spiehl, R. Hoffmann, R. Precht and K. Bonrad, *Thin Solid Films*, 2016, **600**, 59-64.
41 D. E. Walker, M. Major, M. Baghaie Yazdi, A. Klyszcz, M. Haeming, K. Bonrad, C. Melzer, W. Donner and H. von Seggern, *ACS Appl. Mater. Interfaces*, 2012, **4**, 6834-6840.
42 C. H. Kim, Y. S. Rim and H. J. Kim, *ACS Appl. Mater. Interfaces*, 2013, 5, 6108-6112.
43 N. Djourelov, Y. Aman, K. Berovski, P. Nedelec, N. Charvin, V. Garnier and E. Djurado, *Phys. Status Solidi A*, 2011, **208**, 795-802.
44 V. P. Shantarovich, I. B. Kevdina, N. F. Miron, Y. V. Baronova, S. S. Berdonosov, S. B. Baronov and I. V. Melikhov, *Inorg. Mater.*, 2005, **41**, 255-260.
45 G. Molnar, J. Borossay, M. Benabdesselam, P. Iacconi, D. Lapraz, K. Suvegh and A. Vertes, *Phys. Status Solidi A*, 2000, **179**, 249-260.
K. P. Muthe, K. Sudarshan, P. K. Pujarai, M. S. Kulkarni, N. S. Rawat, B. C. Bhatt and S. K. Gupta, *J. Phys. D-Appl. Phys.*, 2009, **42**, 105405.

